

Supporting Information

Water-soluble pH-switchable cobalt complexes for aqueous symmetric redox flow batteries

Hao Wang,^{†,‡} Sayed Youssef Sayed,^{†,‡} Yuqiao Zhou,[†] Brian C. Olsen,^{†,‡} Erik J. Luber,^{†,‡}
and Jillian M. Buriak^{†,‡,*}

[†]Department of Chemistry, University of Alberta, 11227 Saskatchewan Drive, Edmonton,
AB T6G 2G2, Canada.

[‡]Nanotechnology Research Center, National Research Council Canada, 11421
Saskatchewan Drive, Edmonton, AB T6G 2M9, Canada.

*E-mail: (J.M.B) jburiak@ualberta.ca

Section S1: Experimental Methods

- Chemicals and instruments
- Synthesis of 2,6-Bis[1-(4-carboxyphenylimino)ethyl]pyridine (BCPIP).
- Synthesis of 2,6-Bis[1-(4-carboxyphenylimino)ethyl]pyridine cobalt(II) chloride (BCPIP-Co)
- UV-vis Studies
- Solubility tests
- Electrochemical studies
- Full cell performance

Section S2: Determination of kinetic parameters

Section S3: Supplemental Figures, Table, Scheme

Section S4: Crystallographic data for BCPIP-Co

REFERENCES

Section S1: Experimental Methods

Chemicals and instruments. All the chemicals were purchased from Sigma-Aldrich or Alfa Aesar and used directly without further purification. Milli-Q water was sparged with Ar for 2 h before use. ^1H and ^{13}C NMR spectra were recorded on an Agilent VNMRS (700 MHz) spectrometer and referenced to DMSO (δ 2.49 ppm) for ^1H NMR. UV-vis spectra were collected with a Perkin Elmer Lambda 1050 UV-Vis-NIR spectrophotometer (Figure S4). A VWR Symphony SB70P pH meter was used for pH measurements. The SEM images were taken with a ZEISS SIGMA field emission scanning electron microscope. Mass spectra were obtained using an Agilent 6220 oaTOF in electrospray mode. Solution magnetic susceptibilities were measured by the Evans method.¹ The FTIR sample was prepared by spin-casting on the surface of a shard of an native oxide-capped silicon wafer. The FTIR spectra were obtained using a Nicolet Nexus 760 spectrometer with a liquid nitrogen-cooled MCT detector and a nitrogen-purged sample chamber in transmission mode. Elemental analysis was acquired on a Thermo Flash 2000 Elemental Analyzer. X-ray crystallographic details are described in Section S4. All cyclic voltammograms were recorded with a Biologic Science Instruments VSP multichannel potentiostat using EC-Lab V11.20 software and referenced vs. Ag/AgCl reference electrode (3 M NaCl). Detailed procedures for electrochemical kinetic study and redox flow battery cycling experiments are described below.

Synthesis of 2,6-Bis[1-(4-carboxyphenylimino)ethyl]pyridine (BCPIP). 2,6-Diacetylpyridine (2.7 g, 14.6 mmol) and *p*-aminobenzoic acid (5 g, 36.4 mmol) were dissolved in 300 ml of dry xylene. The reaction mixture was heated to reflux under Ar for 2 d with constant stirring. A Dean-Stark trap was applied to remove water and 65 ml of xylene every 12 h (total 260 ml). After 2 d, the mixture was cooled to room temperature, and the residual solvent was removed under reduced pressure. The solid residue was washed with methanol to yield 5.99 g of a light yellow powder after drying under vacuum. The yield was ca. 93%. ^1H NMR (DMSO- d_6 , 499.801 MHz, 27 °C): δ (in ppm), 2.33 (s, 6H), 6.95 (d, 4H), 7.95 (d, 5H), 8.07 (t, 1H), 8.32 (d, 2H), 12.73 (s, 2H). ^{13}C

NMR (DMSO- d_6 , 125.689 MHz, 27 °C): δ (in ppm), 16.16, 119.00, 122.68, 125.93, 130.56, 137.74, 154.40, 154.89, 166.84, 167.01. ESI-MS, m/z: 400 [BCPIP - H]⁻.

Synthesis of 2,6-Bis[1-(4-carboxyphenylimino)ethyl]pyridine cobalt(II) chloride (BCPIP-Co). BCPIP (1 g, 2.49 mmol) and CoCl₂·6H₂O (0.295 g, 1.25 mmol) were combined in 75 ml of methanol and stirred at room temperature for 1 h. The solvent was then removed under reduced pressure. The dark red solid was washed with acetonitrile and vacuum-dried at room temperature. The yield was 95%. Elemental analysis calc. for C₄₆H₃₈CoN₆O₈, Theoretical: C = 59.25, H = 4.07, N = 9.01. Measured: C = 58.86, H = 4.07, N = 8.87. ESI-MS, m/z: 430 [BCPIP-Co - 2 Cl]⁺², 860 [BCPIP-Co - 2 Cl]⁺. Magnetic susceptibility (methanol- d_4 , 27 °C): $\mu_{\text{eff}} = 2.44 \mu_B$.

UV-vis Studies. The UV-vis spectra of BCPIP-Co(II) under different pH values were taken with an aqueous solution of 0.02 mM of BCPIP-Co(II) in 0.5 M NaCl (aq). The pH values were adjusted using aqueous 0.1 M NaOH and 0.1 M HCl solutions. The solution, after adjustment, was allowed to equilibrate for at least 4 min.

Solubility tests. The solubility limit of BCPIP-Co(II) was measured by adding the BCPIP-Co(II) in water until no further solid could be dissolved, at room temperature. The saturated solution was obtained by filtering the mixture through a 0.2 μm PTFE syringe filter. The saturated solution was then diluted and evaluated by UV-Vis spectrophotometer (PerkinElmer Lambda 1050 UV-Vis-Nir spectrophotometer). A pre-calibrated absorbance-concentration curve with a known concentration of BCPIP-Co(II) was used to calculate the maximum concentration (Figures S13 and S14).

Electrochemical studies. Cyclic voltammetry (CV) and rotating disk electrode (RDE) tests were performed on Biologic Science Instruments VSP multichannel potentiostat using three-electrode set-up with a glassy carbon electrode (3 mm for CV studies and 5 mm for RDE studies), a platinum counter electrode and an Ag/AgCl reference electrode. All electrochemical studies were conducted in 0.5 M NaCl (aq) electrolyte solutions under Ar atmosphere. The working electrode was polished with 1 micron and 0.05-micron alumina powder and rinsed with Milli-Q water before each experiment. CV curves were recorded at a sweep rate of 50 mV/s or specific rates where indicated. The pH values were adjusted by aqueous HCl or NaOH solutions.

Full cell performance. These tests were carried out using a Biologic Science Instruments VSP multichannel potentiostat and a flow cell. The flow cell for BCPIP-Co was constructed with a zero-gap flow cell from Fuel Cell Tech comprised of POCO graphite flow plates with a serpentine flow pattern in combination with 10 cm² geometric surface area electrodes stacked of pieces of carbon paper (Sigracet SGL 29AA) on each side. The carbon paper was pretreated under oxygen plasma using plasma cleaner (Harrick PDC 32G, 18 W) at 0.8 Torr for 6 min to create a hydrophilic surface (Figures S17, S18). Viton gaskets were used to achieve ~20% compression of the carbon papers. A sheet of pretreated anion exchange membrane (fumasep FAS-30, Fumatech, Germany), which had been stored in 1 M NaCl (aq) overnight, was sandwiched between carbon papers. Two glass reservoirs were filled with 10 ml of 0.5 M NaCl (aq) electrolytes containing certain concentration of active materials. A peristaltic pump (Cole-Parmer Masterflex L/S) was used to feed the electrolytes were into the flow cell through Viton tubing at a rate of 60 ml/min. The specific capacity was calculated based on the mass of BCPIP-Co. Both reservoirs were purged with argon and sealed before cell cycling. The cell was galvanostatic charged/discharged between 1.13 V and 0 V at a current of 20 mA. EIS was conducted from 99 kHz to 6 Hz using a 10 mV sine perturbation at 50% SOC.

Section S2: Determination of kinetic parameters

For RDE experiments, a Pine Instrument ASR rotator was used to control the rotation speed. Linear sweep voltammetry studies were carried out at a rate of 5 mV/s when the disk electrode was rotated at a specific speed. The limiting current $i_{l,a}$ measured at 0.86 V were plotted versus the rotation rate (ω). The Levich plot showed a linear relationship between limiting current and square root rotation rate. The slope of the fitted line is defined by the Levich equation,

$$i_{l,a} = (0.62nFAD^{\frac{2}{3}}\nu^{-\frac{1}{6}}C_o)\sqrt{\omega} \quad (S1)$$

where n is the number of electrons involved, F is the Faraday's constant, A is the electrode area, C_o is the concentration of BCPIP-Co, and ν is the kinematic viscosity (0.01024 cm²/s for 0.5 M NaCl). The diffusion coefficient, D , of BCPIP-Co was calculated from the Levich equation.

A series of plots of reciprocal of square root rotation rate versus measured current at different overpotentials were extrapolated to infinite rotation rate to obtain kinetic current (i_k , without mass transfer effect) based on Koutecký–Levich equation,

$$\frac{1}{i_m} = \frac{1}{i_k} + \frac{1}{i_{l,a}} = \frac{1}{i_k} + \frac{1}{(0.62nFAD^{\frac{2}{3}}\nu^{-\frac{1}{6}}C_o)\sqrt{\omega}} \quad (S2)$$

where i_m is the measured current, $i_{l,a}$ is the limiting current as previously defined by Equation S1. Using these values of kinetic current as a function of overpotential, the rate constant k^0 is determined using the current-potential equation,²

$$\log_{10}(i_k) = -\frac{\alpha nF(E - E^0)}{RT} \log_{10}(e) + \log_{10}(nFAC_0^{\text{bulk}}k^0) \quad (S3)$$

where E is the electrode potential, E^0 is the formal electrode potential, α is the charge transfer coefficient (assumed to be equal to 0.5), n is the number of electrons involved in the reaction, F is Faraday's constant, R is the ideal gas constant, T is the temperature, A is the electrode area and C_0^{bulk} is the bulk concentration of BCPIP-Co(II). The rate constant k^0 , is determined from the x-intercept of fitting a straight line through a plot of

$\log_{10}(i_k)$ vs $E - E^0$. All the electrochemical experiments were performed three times at room temperature.

Nicholson's analysis is another classic and frequently used method to estimate rate constants for quasi-reversible systems. The peak to peak separation ΔE_p is only a function of dimensionless kinetic parameter, ψ when $0.3 < \alpha < 0.7$. The corresponding relations between ψ and ΔE_p can be obtained from the table in the original paper.³ Due to the discrete points in the table, for practical usage, Equation S4 is used to roughly estimate ψ .⁴

$$\psi = \frac{-0.6288 + 0.0021\Delta E_p}{1 - 0.017\Delta E_p} \quad (S4)$$

Following this, the Nicholson equation (Equation S5) was applied to calculate k^0 . It is assumed that $D_O = D_R$ and $\alpha = 0.5$

$$\psi = \frac{(D_O/D_R)^{\alpha/2} k^0}{\sqrt{\pi D_O n F v / RT}} \quad (S5)$$

Section S3: Supplemental Figures

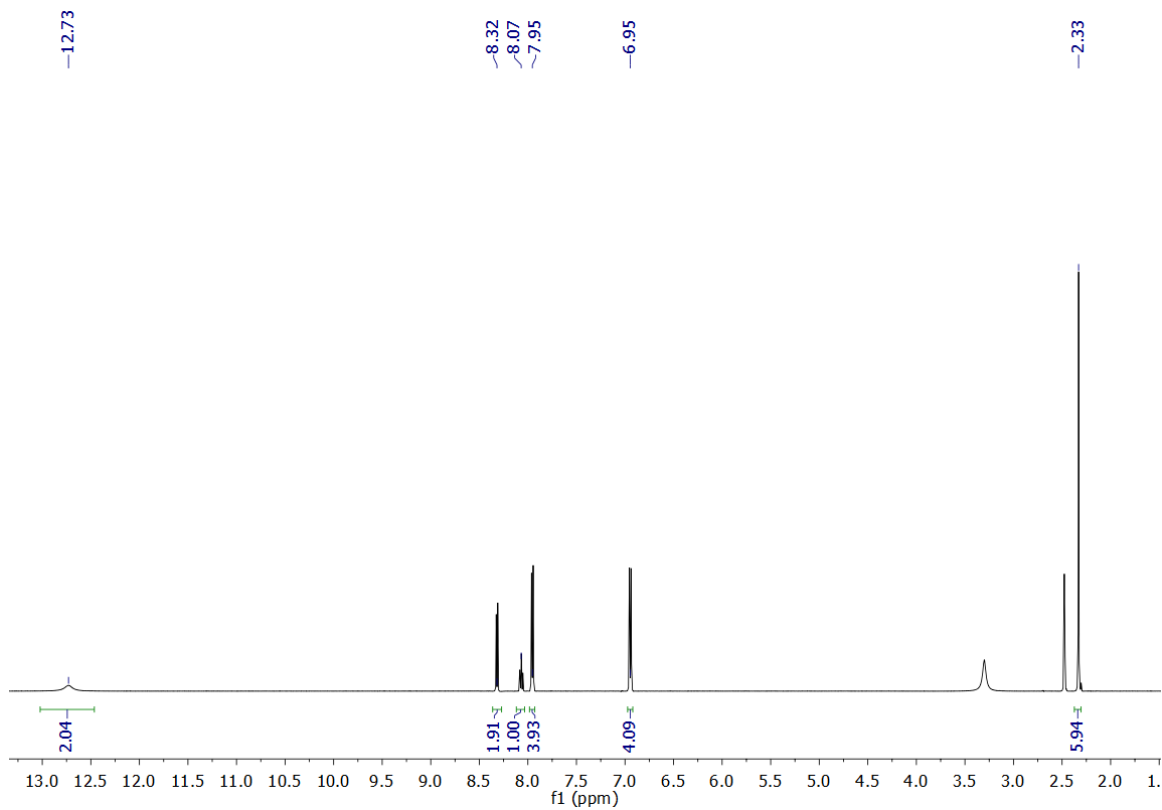


Figure S1. ^1H NMR spectrum of the ligand, BCPIP (DMSO-d_6 , $27\text{ }^\circ\text{C}$).

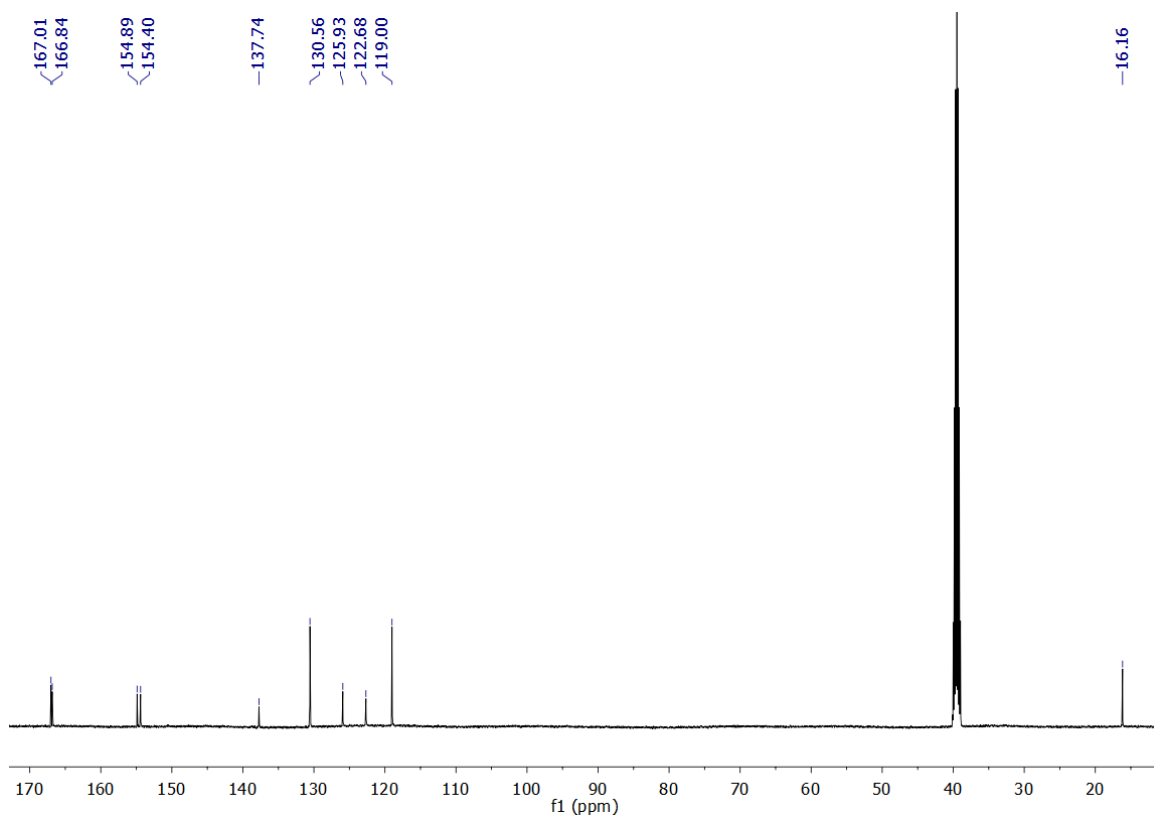


Figure S2. ^{13}C NMR spectrum of the ligand, BCPIP (DMSO-d_6 , $27\text{ }^\circ\text{C}$).

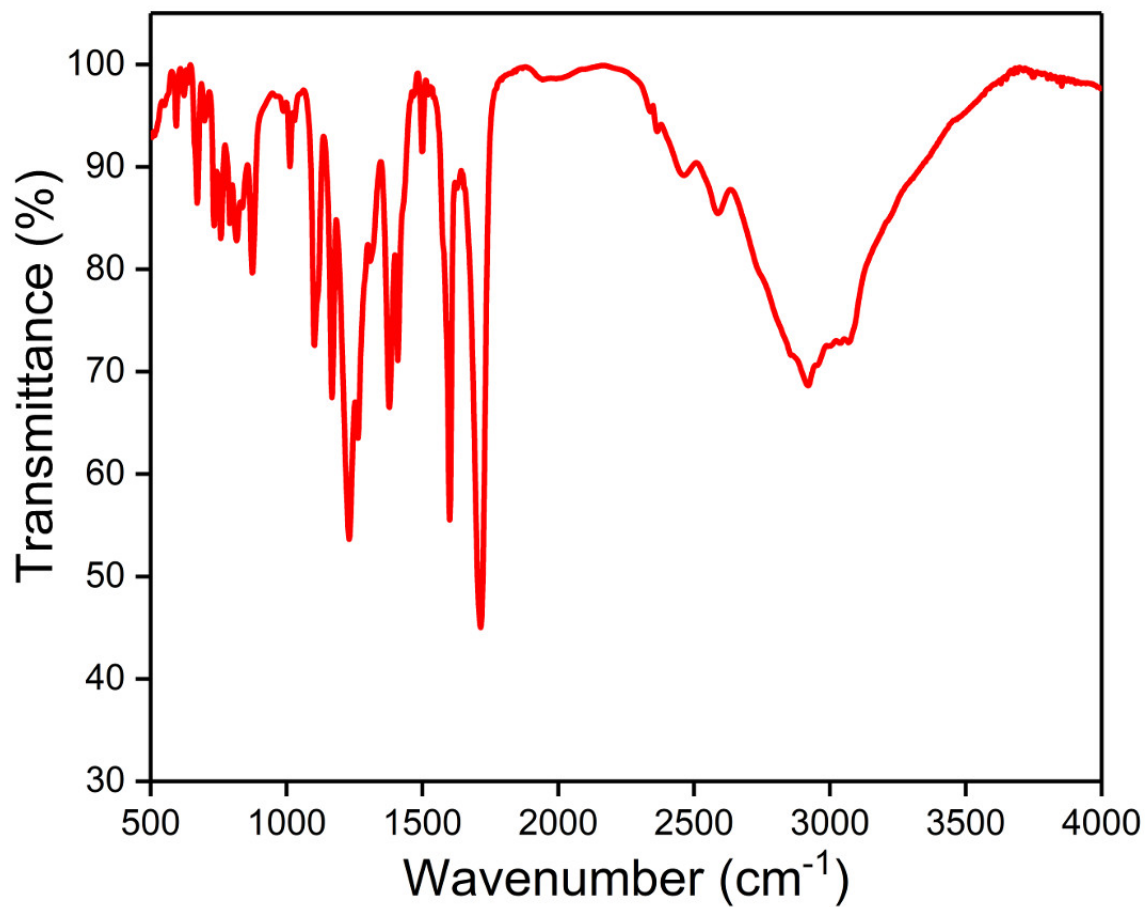


Figure S3. Transmission mode FTIR spectra of BCPIP-Co(II) on a native oxide-capped silicon wafer. Features at 1600 and 1575 cm⁻¹ correspond to pyridyl and aryl-ring breathing mode deformations.

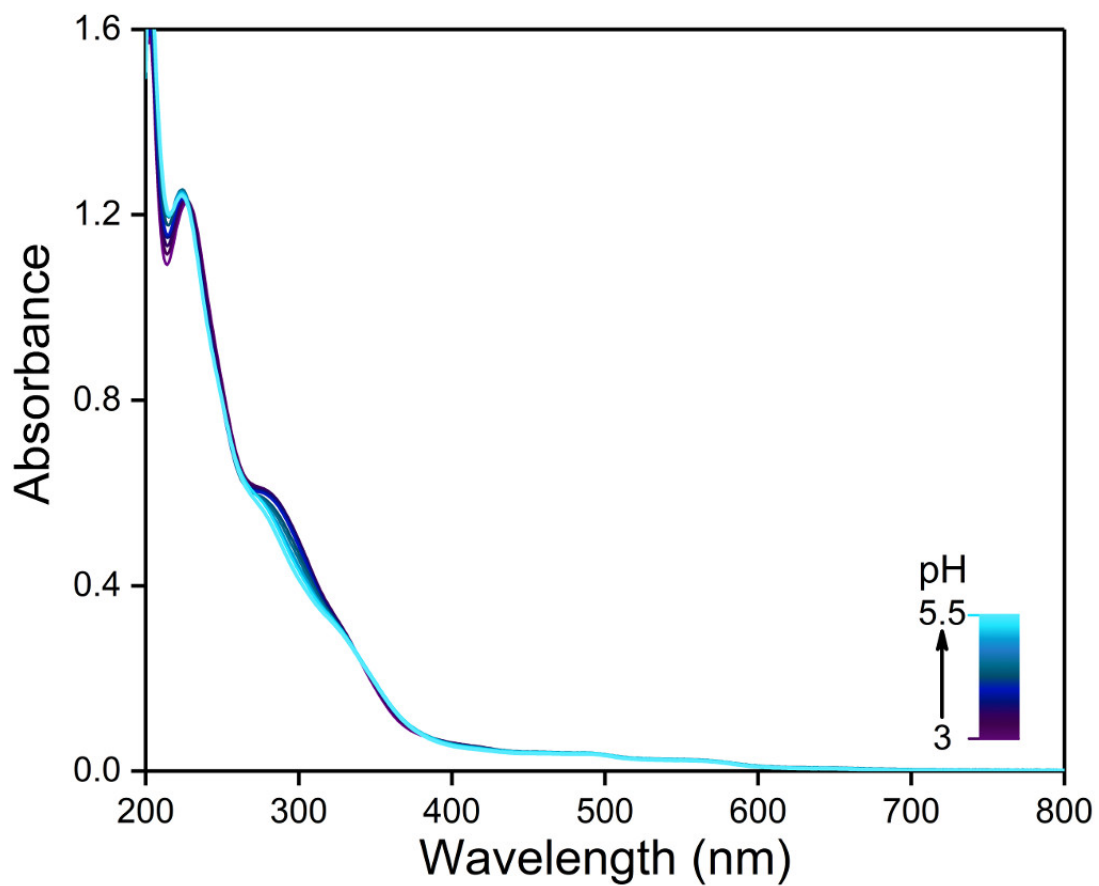


Figure S4. UV spectra of BCPIP-Co(II) at different pH values (0.02 mM) using NaOH (aq) to adjust pH.

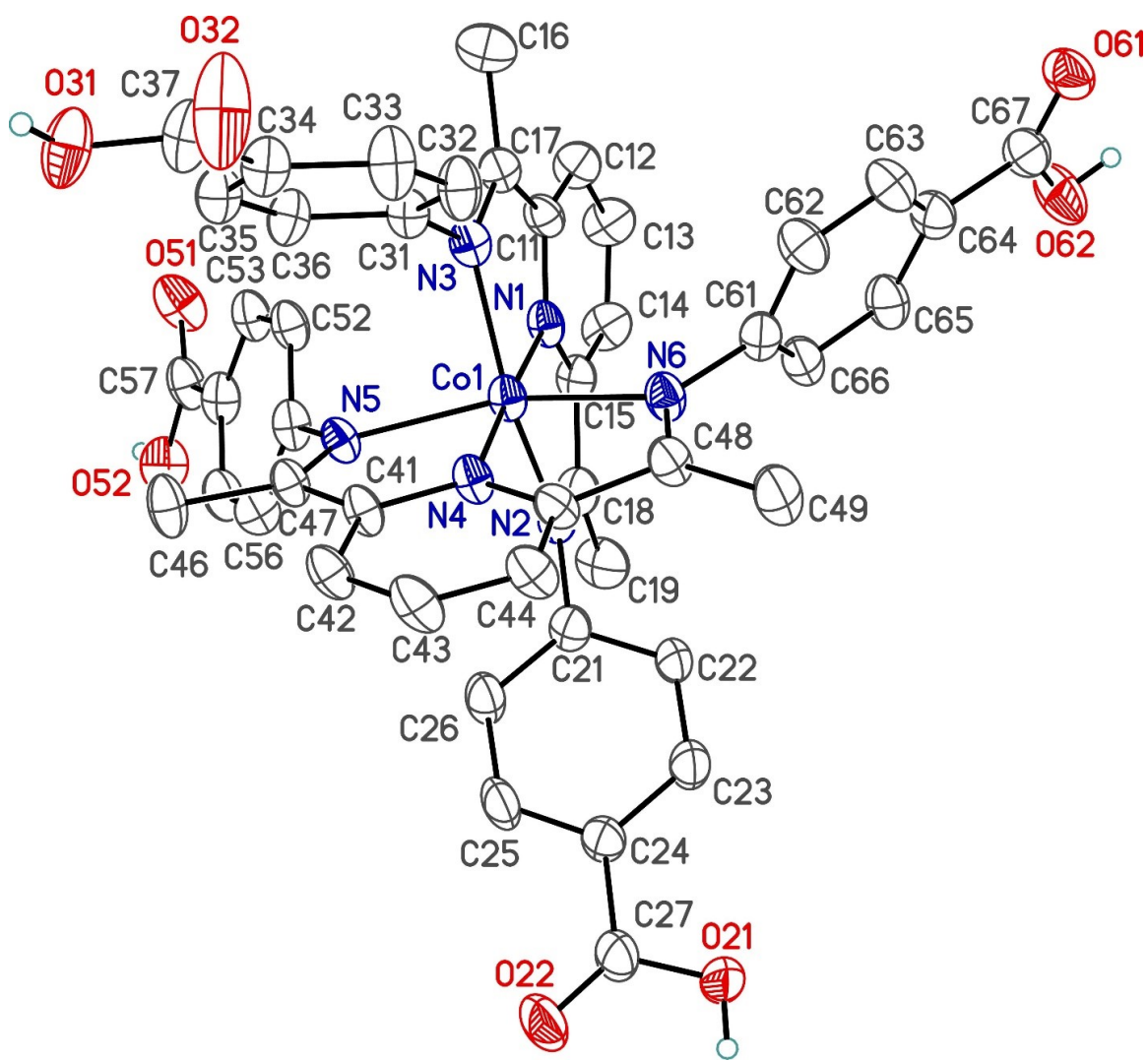


Figure S5. Perspective view of the *Moiety A* of 2,6-Bis[1-(4-carboxyphenylimino)ethyl]pyridine cobalt(II) chloride showing the atom labelling scheme. Non-hydrogen atoms are represented by Gaussian ellipsoids at the 30% probability level. Hydrogen atoms are shown with arbitrarily small thermal parameters for carboxylic units. Selected interatomic distances (Å): Co1–N1 1.863(4), Co1–N2 2.014(5), Co1–N3 2.000(5), Co1–N4 1.915(4), Co1–N5 2.138(5), Co1–N6 2.160(5).

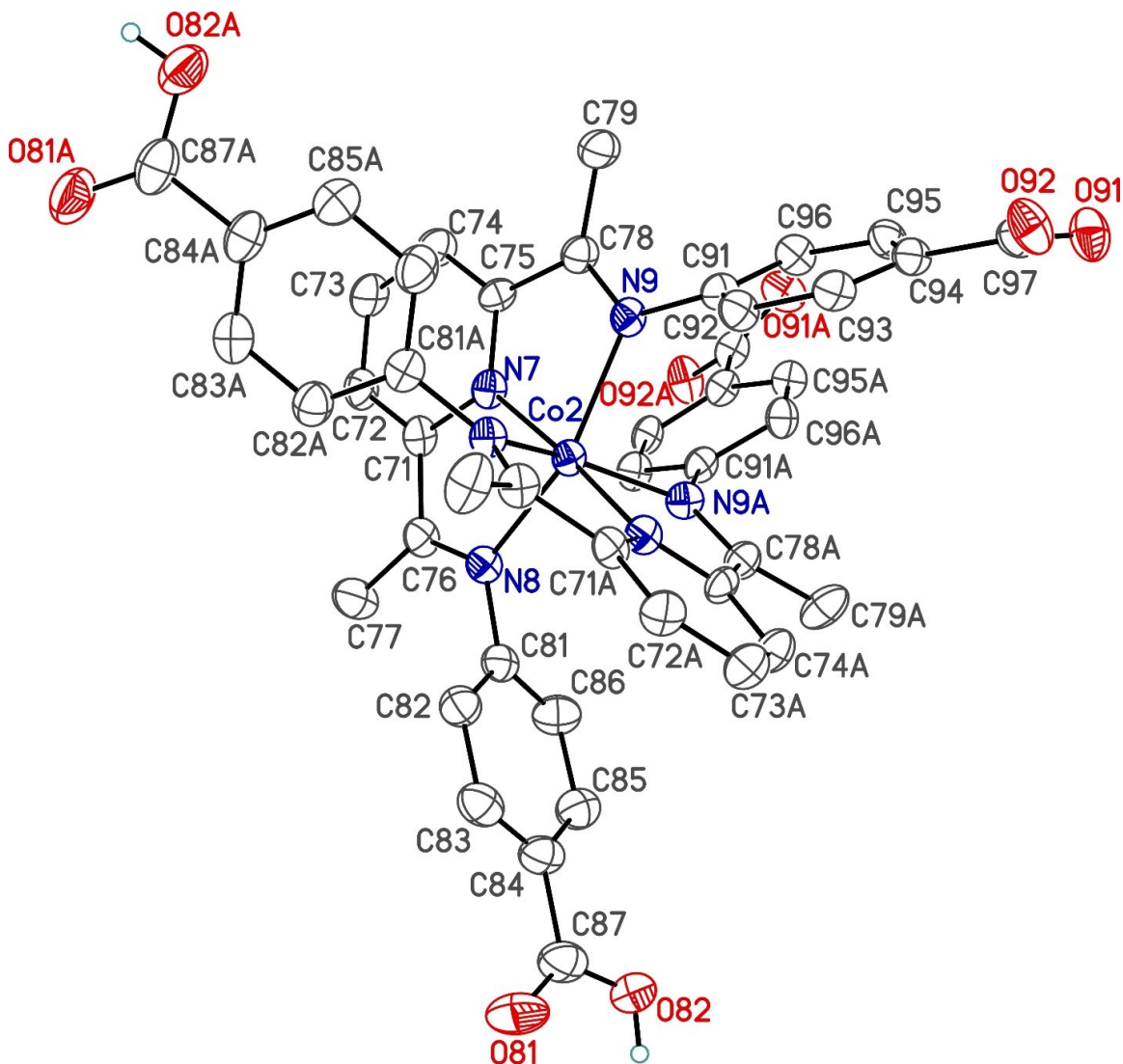


Figure S6. Perspective view of the *Moiety B* of 2,6-Bis[1-(4-carboxyphenylimino)ethyl]pyridine cobalt(II) chloride showing the atom labelling scheme. Non-hydrogen atoms are represented by Gaussian ellipsoids at the 30% probability level. Hydrogen atoms are shown with arbitrarily small thermal parameters for carboxylic units. Selected interatomic distances (Å): Co2–N7 1.894(4), Co2–N8 2.049(5), Co2–N9 2.102(5).

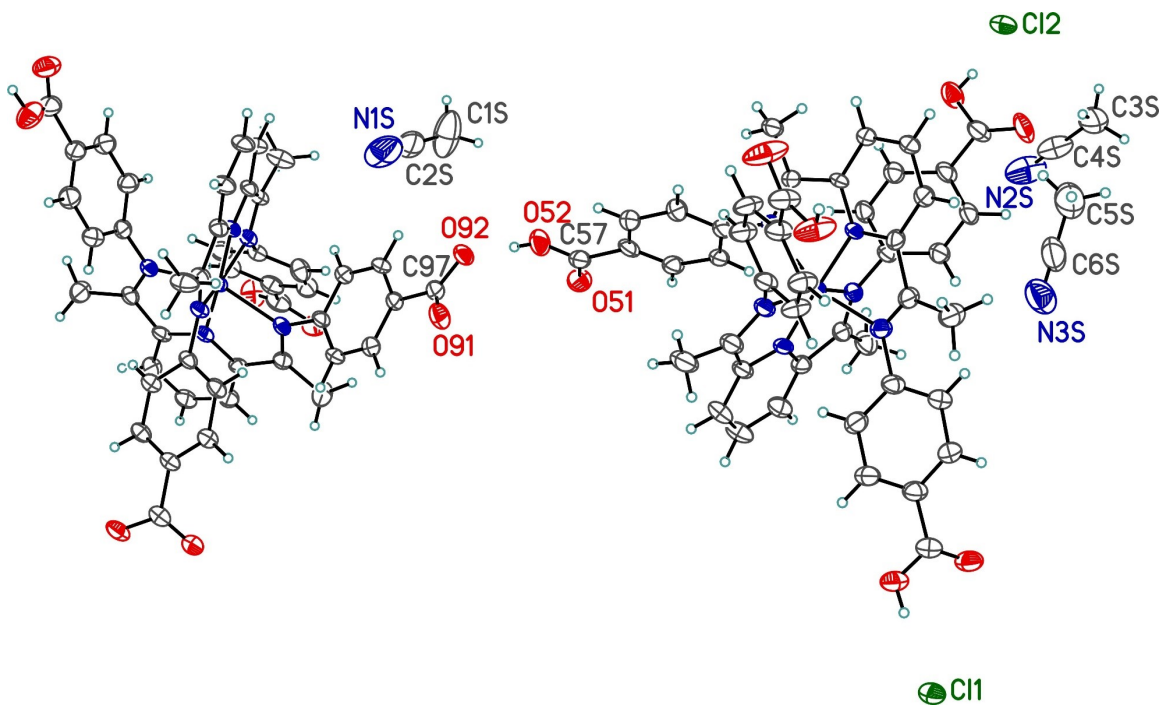


Figure S7. Perspective view of the whole contents of 2,6-Bis[1-(4-carboxyphenylimino)ethyl] pyridine cobalt(II) chloride, 2,6-Bis[1-(4-carboxyphenylimino)ethyl] pyridine cobalt(II) chloride, acetonitrile solvate showing the atom labelling scheme. Non-hydrogen atoms are represented by Gaussian ellipsoids at the 30% probability level. Hydrogen atoms are shown with arbitrarily small thermal parameters.

In order to investigate the reversibility of the protonation/deprotonation of the carboxylic acid groups for the BCPIP-Co(II) complex, the CV was run at pH 3 and the pH then increased to 5.5, followed by lowering back down to pH 3.0. As shown in Figure S17, the CVs for the Co(II)/Co(I) and Co(II)/Co(III) redox reactions at pH 3.0 before and after raising the pH are superimposed. Thus, under these conditions, the complex is chemically and electrochemically stable upon deprotonation and protonation of the carboxylic acid/carboxylate groups in this range.

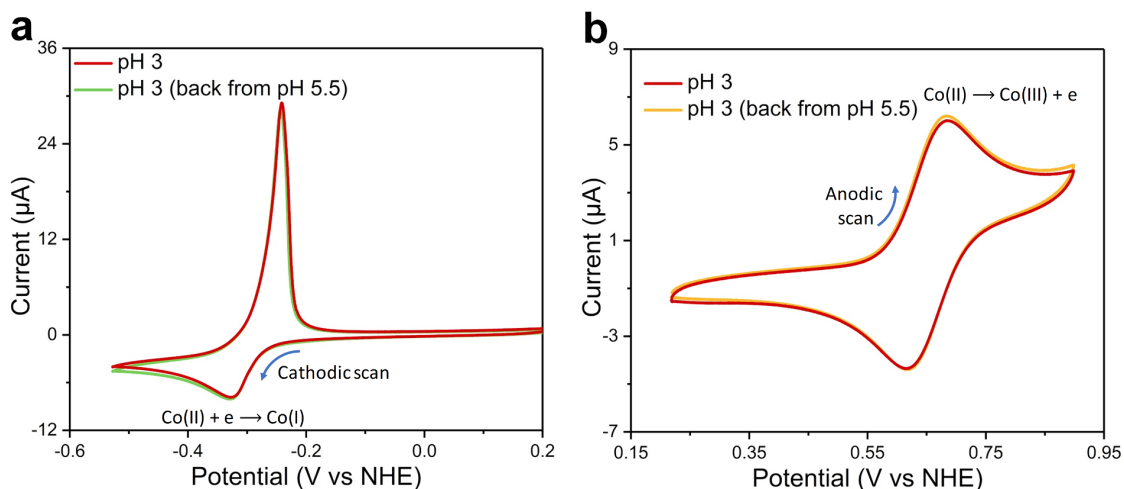


Figure S8. CV of 1 mM of BCPIP-Co(II) on a glassy carbon electrode in 0.5 M NaCl (aq) at pH 3.0, and after increasing the pH to 5.5, and lowering it back to pH 3.0. (a) Cathodic event [Co(II/I)] for the BCPIP-Co(II) redox reactions. (b) Anodic event [Co(II/III)] for the BCPIP-Co(II) redox reactions.

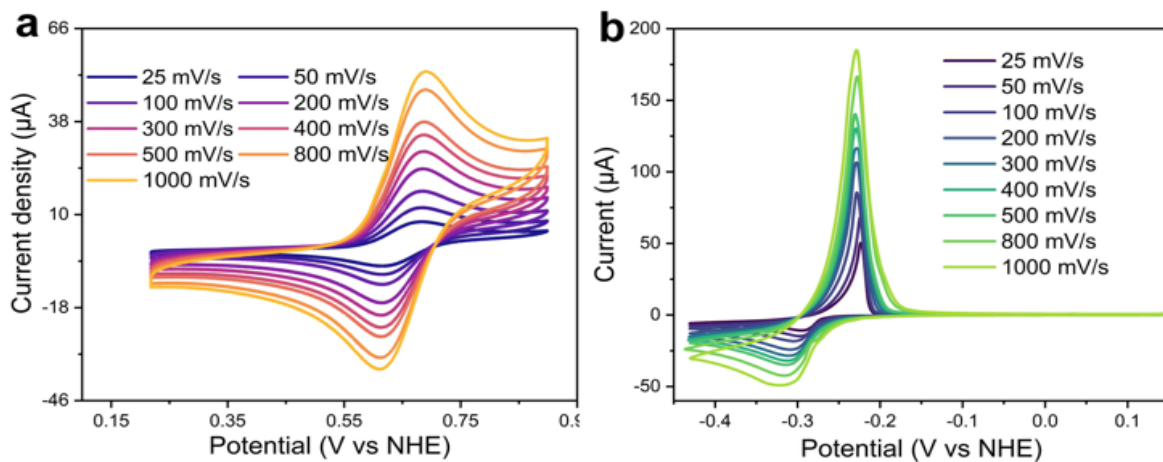


Figure S9. (a) CV curves of 2 mM BCPIP-Co(II-III) at pH 3.0 at various scan rates from 0.025 V/s to 1.0 V/s in 0.5 M NaCl (aq). (b) CV curves of 2 mM BCPIP-Co(II-I) at pH 3.0 at various scan rates from 0.025 V/s to 1.0 V/s in 0.5 M NaCl (aq). The potential axes were corrected for the uncompensated ohmic resistance.

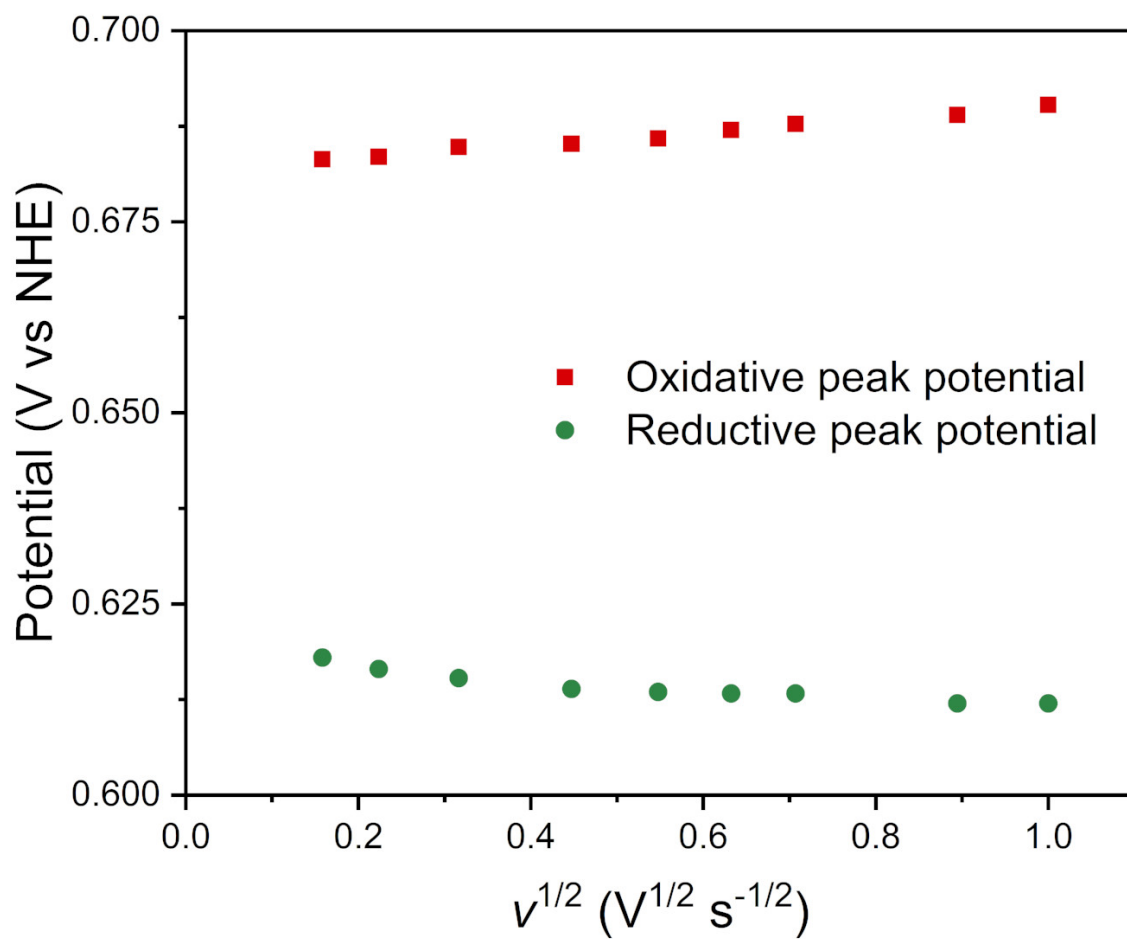


Figure S10. Reductive and oxidative peak potential change with the square root of scan rate $v^{1/2}$ for the corresponding CV curves of BCPIP-Co(II), Co(II/III) redox couple, at pH 3.0.

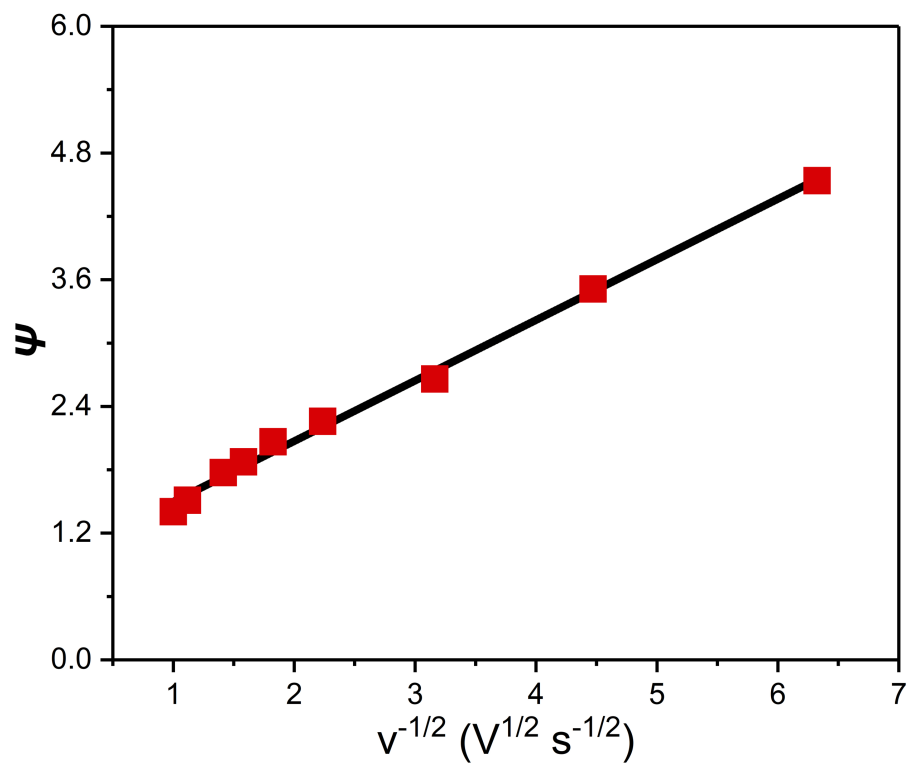


Figure S11. Nicholson's analysis for examination of heterogeneous electron transfer rate constant k^0 : plot of the dimensionless kinetic parameter (Ψ) vs square root of scan rate (v).

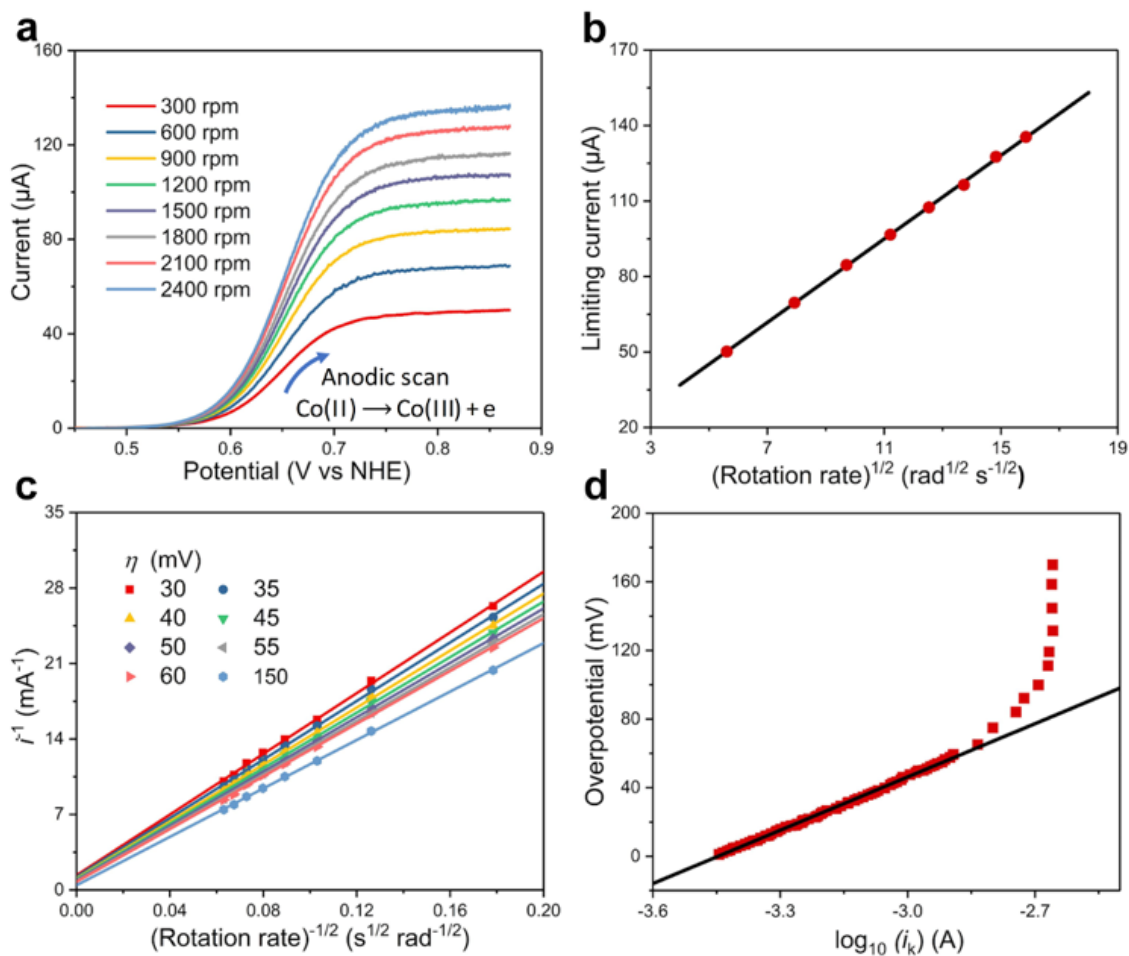


Figure S12. (a) Linear sweep voltammograms for the Co(II)/Co(III) redox reactions of the 2.0 mM BCPIP-Co(II) at different rotation speeds of the RDE in 0.5 M NaCl (aq) at a nominal pH of 3.0. (b) Limiting currents vs. the square root of rotation rate (Levich plots) for BCPIP-Co(II); (c) Koutecký-Levich plot (i^{-1} vs. $\omega^{-1/2}$) of BCPIP-Co(II). (d) Plot of the overpotential vs. $\log_{10}(i_k)$. The overpotential is defined as $E_{\text{meas}} - E^0$.

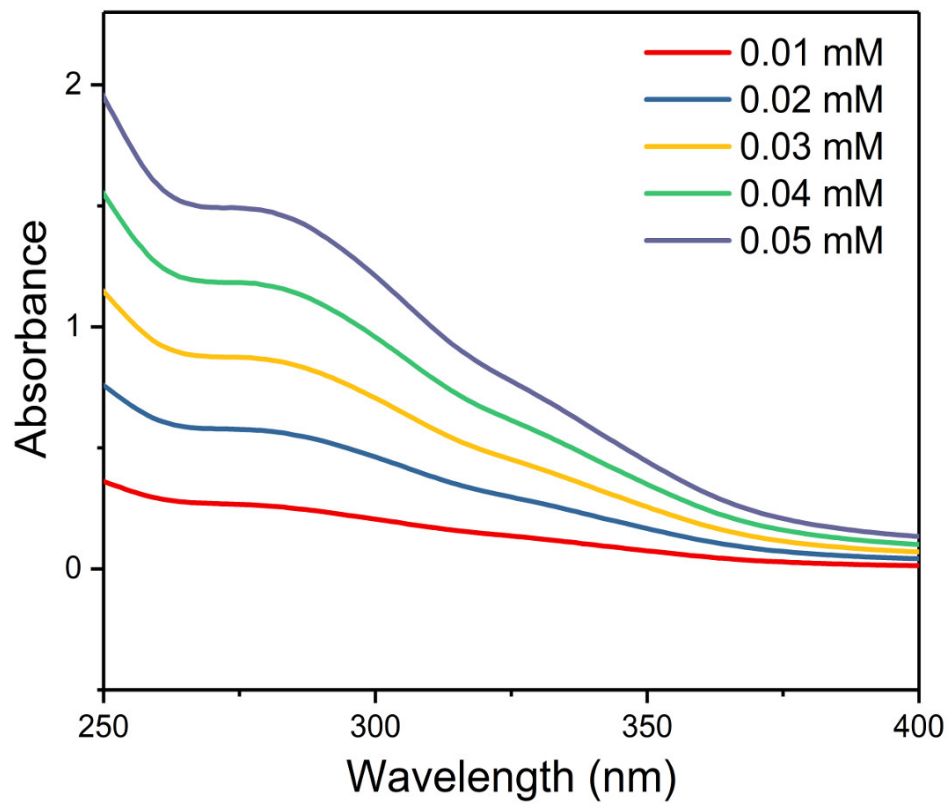


Figure S13. UV-Vis spectra of BCPIP-Co(II) at different concentrations. The solutions were prepared by using ultrapure 18 M Ω ·cm water and the pH was not controlled (the 'native' pH).

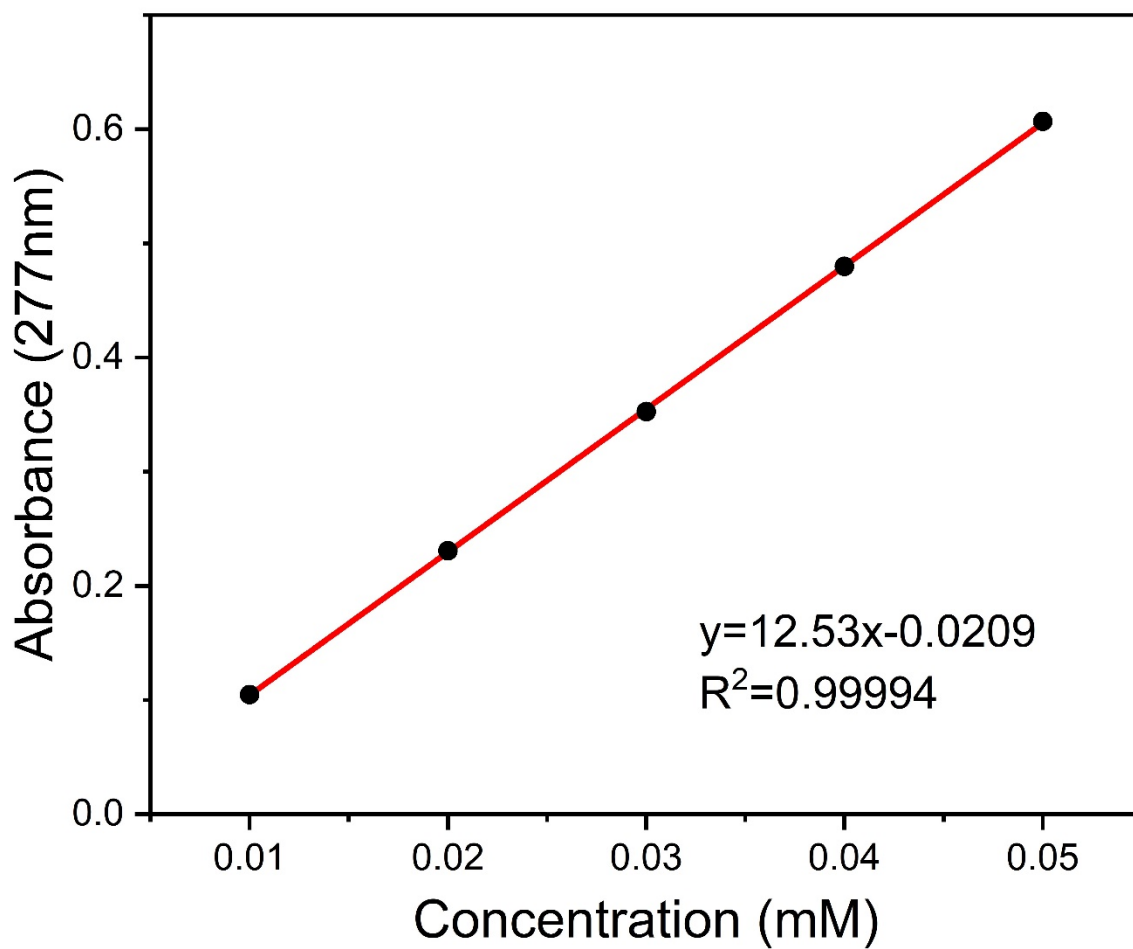


Figure S14. Absorbance at 338 nm as a function of concentration. The solutions were prepared by using ultrapure 18 M Ω ·cm water and the pH was not controlled ('native' pH).

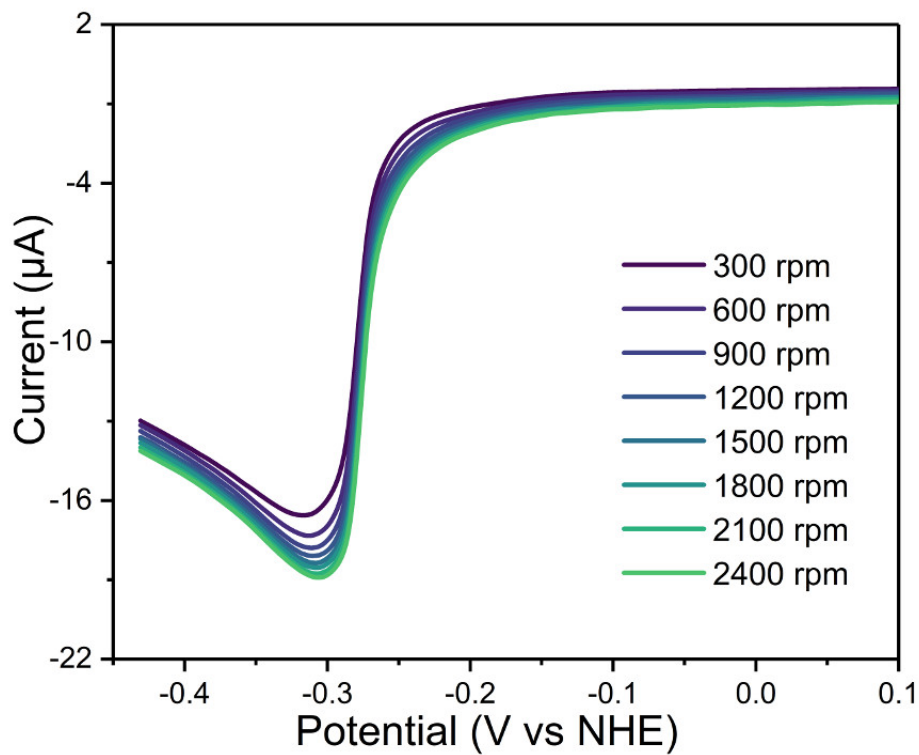


Figure S15. Linear sweep voltammograms of 2.0 mM BCPIP-Co(II), Co(II/I) redox couple, in 0.5 M NaCl (aq) at pH 3.0 under various rotation speeds. Due to the weak interaction between the BCPIP-Co(I) complex with the electrode surface, a peak at *ca.* -0.3 V vs. NHE and seemingly coincident plots are observed in the current-potential region typically used for the mass transfer correction and extraction of kinetic information and thus, impeding further kinetic analysis for the redox reaction [Co(II)/Co(I)] using RDE.

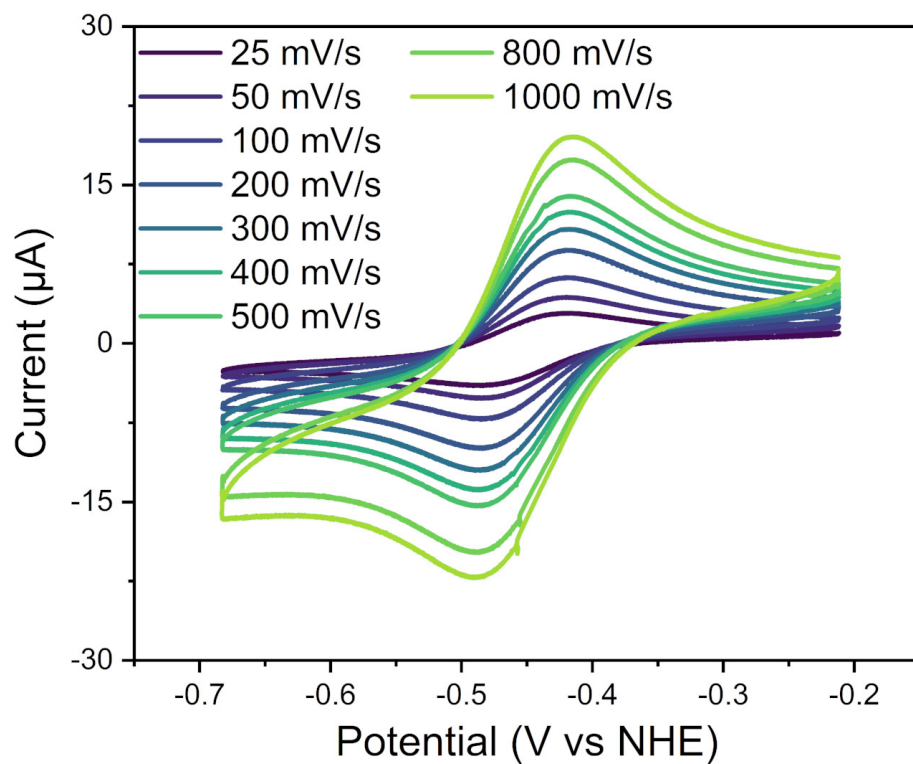


Figure S16. Cyclic Voltammograms of 1 mM BCPIP-Co(II), Co(II/I) redox couple, at various scan rates from 0.025 V/s to 1.0 V/s in 0.5 M NaCl (aq) at pH 5.0.

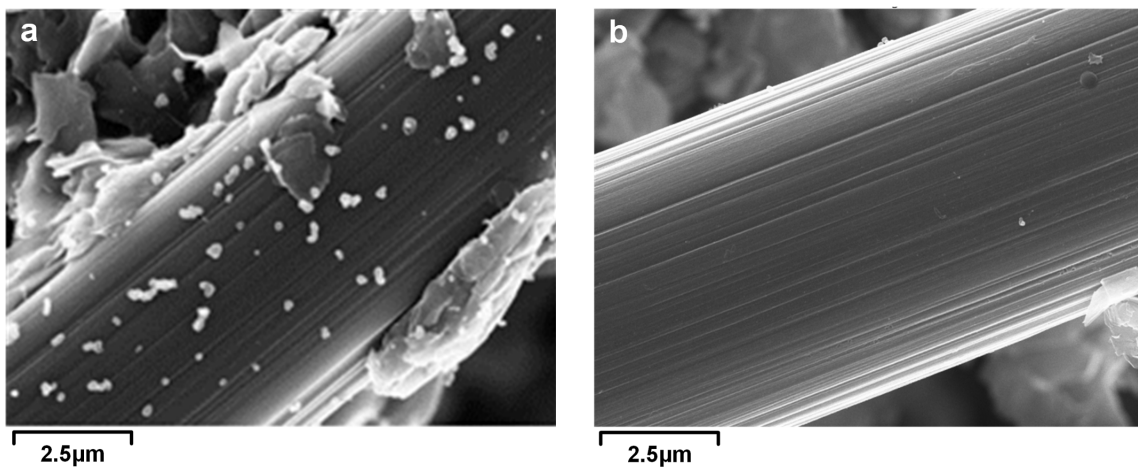


Figure S17. (a) SEM of pristine carbon paper as received from Sigracet 29 AA. (b) SEM of O₂-plasma-pretreated carbon paper. After O₂ plasma, the carbon fibers have fewer scattered particles, and show negligible morphological changes of the carbon fibers themselves.

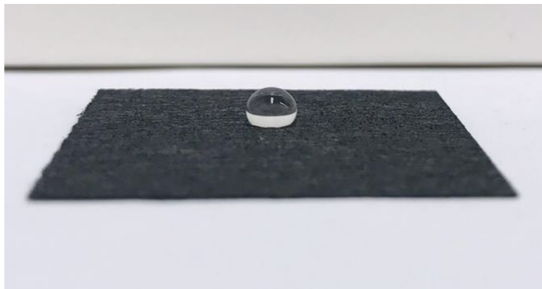
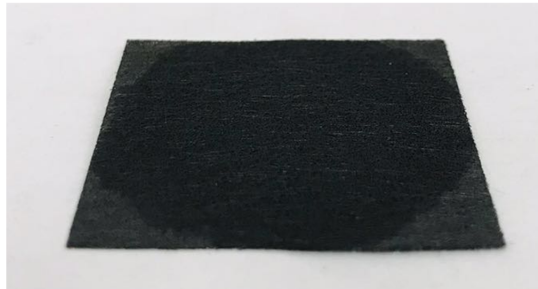
a**b**

Figure S18. Water wetting properties of carbon paper (a) before oxygen plasma (b) after oxygen plasma treatment.

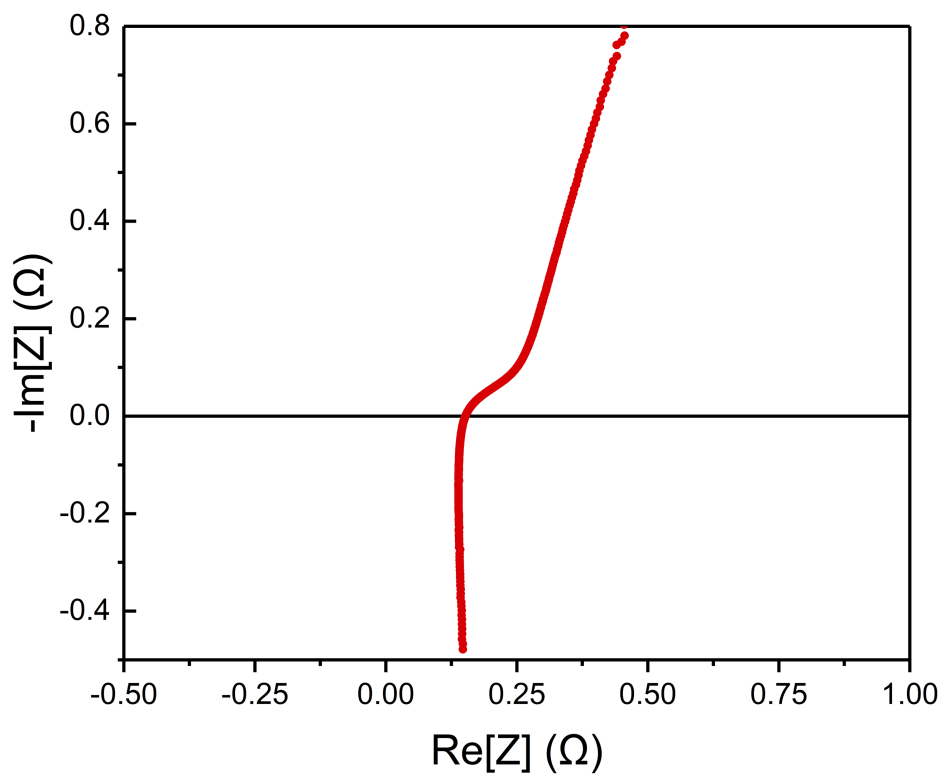


Figure S19. Electrochemical Impedance Spectroscopy (EIS) spectrum of the 1 mM BCPIP-Co(II) symmetric redox flow battery at pH 3.5.

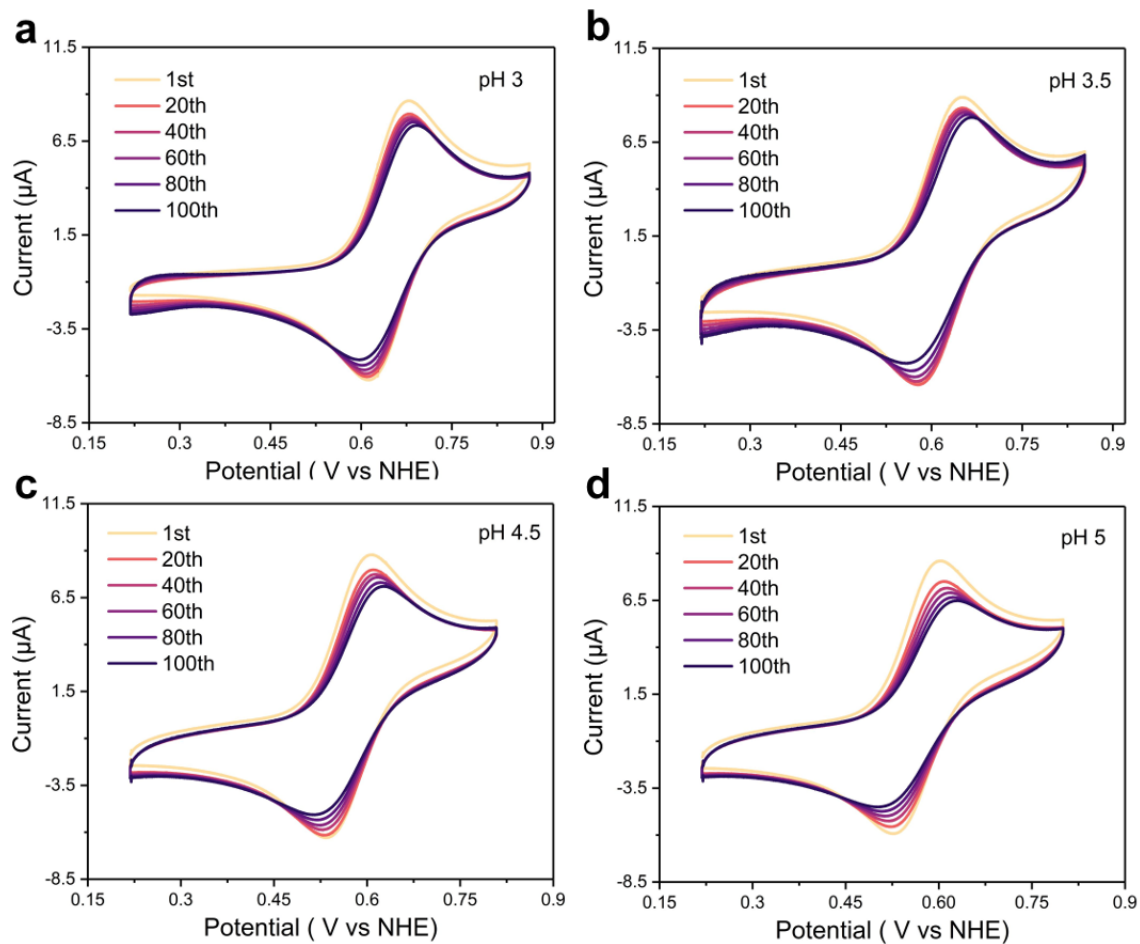


Figure S20. CV curves as a function of cycle number for 1 mM BCPIP(II), Co(II/III) redox couple, in 0.5 M NaCl (aq) at a rate of 100 mV/s for different pH levels. (a) pH 3.0, (b) pH 3.5, (c) pH 4.5 and (d) pH 5.0. The number of cycles is shown as an inset in each panel.

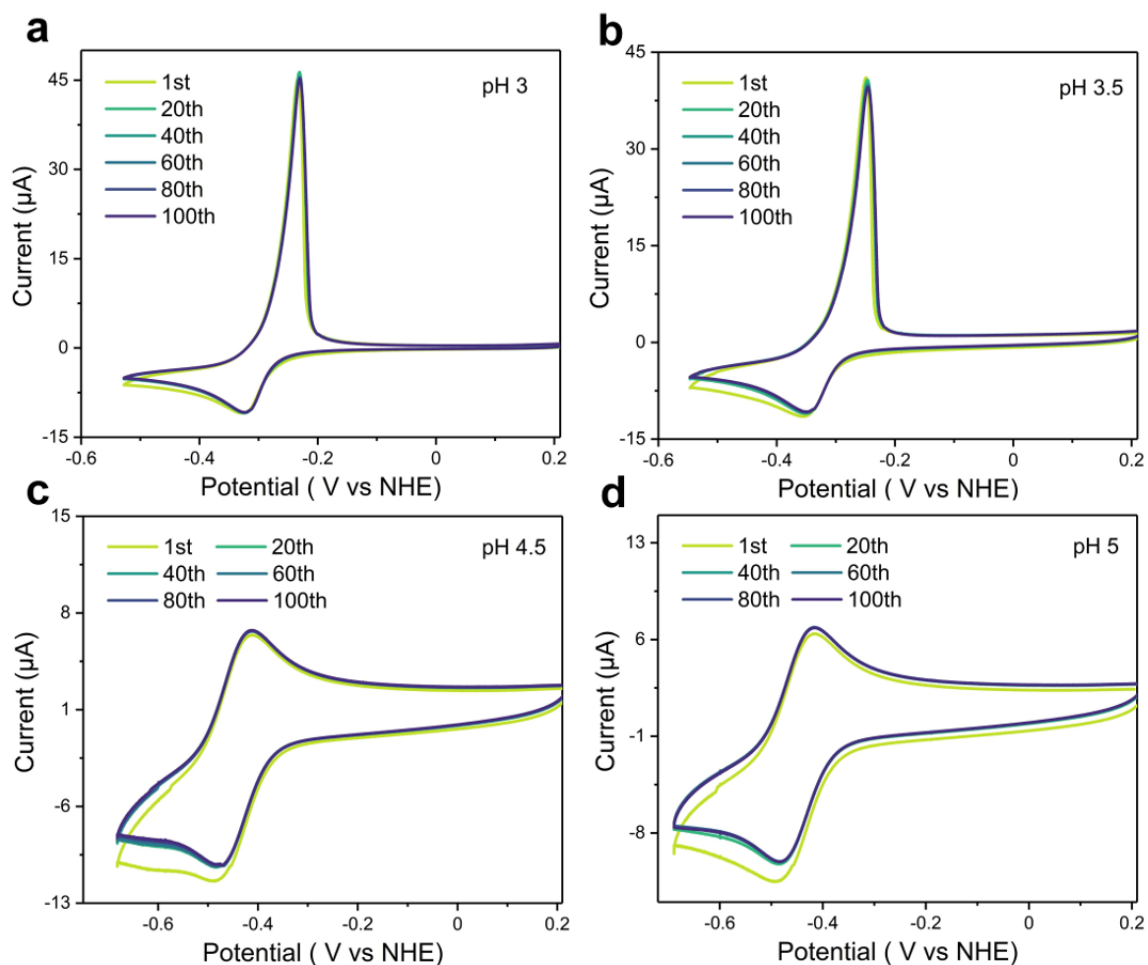


Figure S21. CV curves as a function of cycle number for 1 mM BCPIP(II) , $[\text{Co}(\text{II}/\text{I})]$ redox couple, in 0.5 M NaCl (aq) at a rate of 100 mV/s for different pH levels. (a) pH 3.0, (b) pH 3.5, (c) pH 4.5 and (d) pH 5.0. The number of cycles is shown as an inset in each panel. The number of cycles is shown in the inset in each panel.

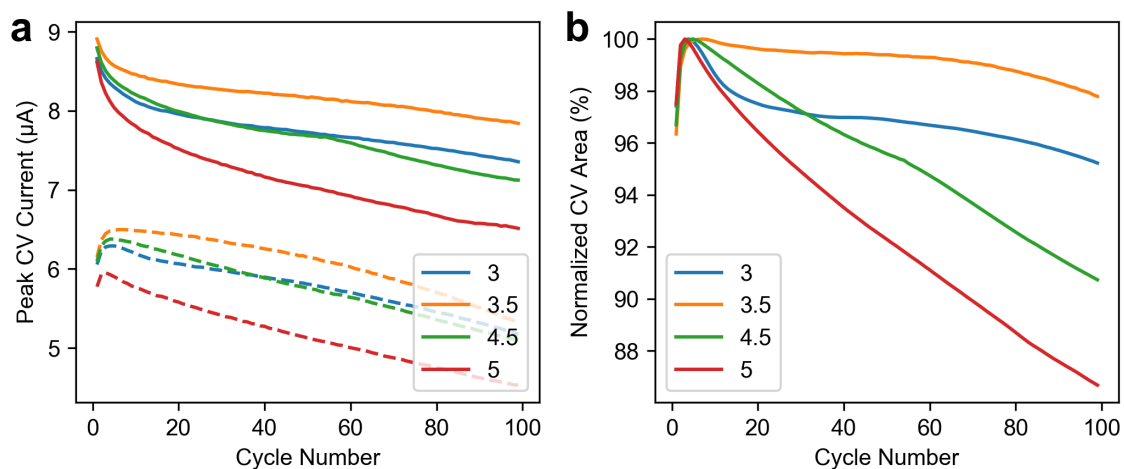


Figure S22. Analyses of peak currents and areas from Figure S10. (a) The absolute values of the peak currents for the anodic (solid lines) and cathodic (dashed lines) sweeps of the 1 mM posolyte CV per cycle. (b) The normalized area is given as a percentage of the area between the anodic and cathodic sweeps of the 1 mM posolyte CV per cycle.

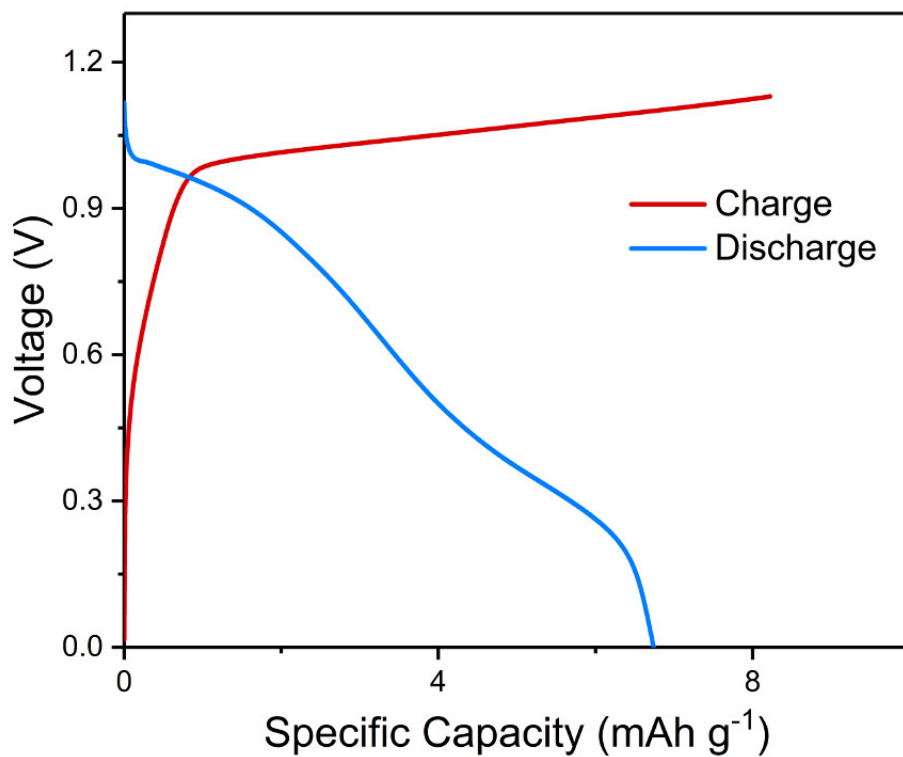


Figure S23. (a) Charge–discharge profile of the 10 mM BCPIP-Co(II) symmetric flow battery at pH 3.5.

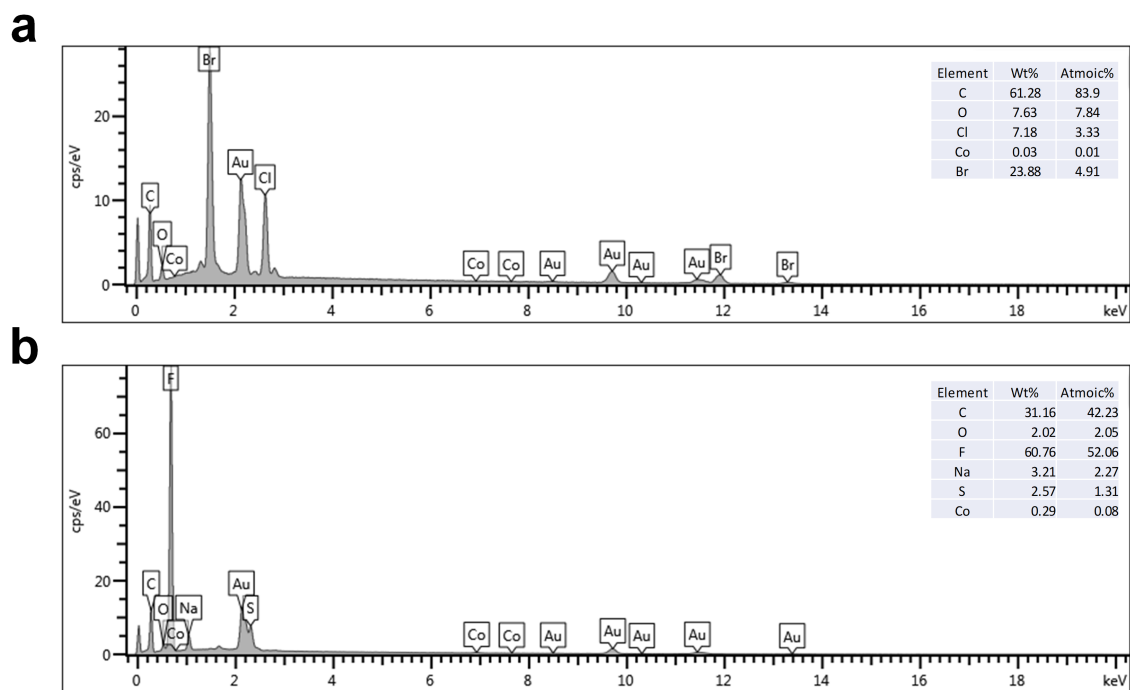


Figure S24. (a) EDX of gold-coated fumasep FAS-30 membrane from the 10 mM BCPIP-Co(II) symmetric cell at pH 3.5 after 100 cycles. (b) EDX of gold-coated Nafion 212 membrane from the 10 mM BCPIP-Co(II) symmetric cell at pH 3.5 after 100 cycles.

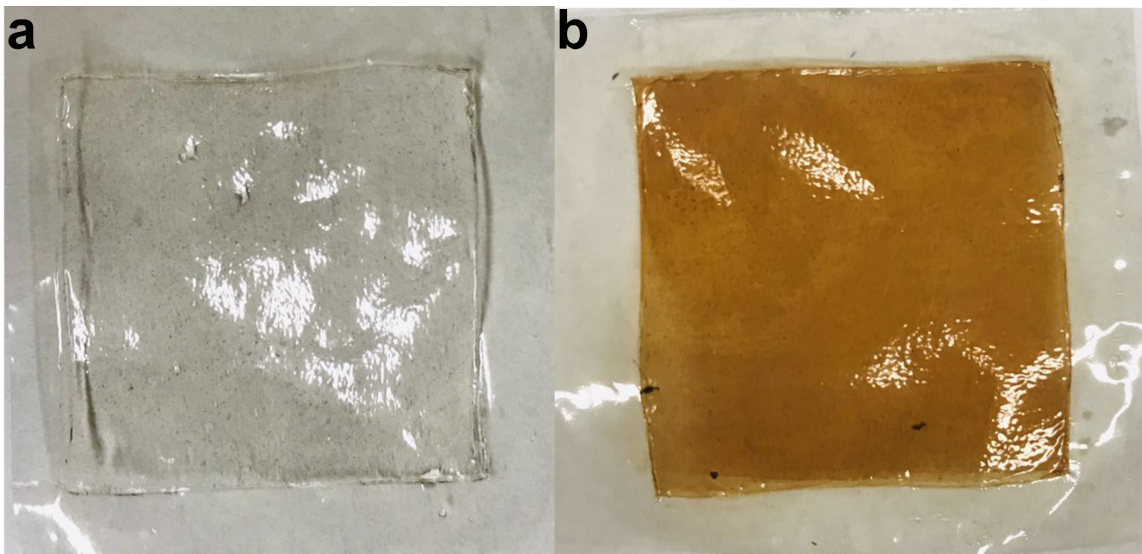


Figure S25. Photographs: (a) Membrane from the 1 mM BCPIP-Co(II) symmetric cell at pH 3.5 after 100 cycles; (b) fumasep FAS-30 membrane from the 10 mM BCPIP-Co(II) symmetric cell at pH 3.5 after 100 cycles.

In the case of 10 mM BCPIP-Co(II) symmetric cell, upon pumping water into the cell, one would expect to observe colourless solutions at the outlets of both the posolyte and negolyte compartments. However, upon rinsing the cell, a colorless solution did emerge from the posolyte side, but a red solution was observed to come out of the negolyte compartment, most likely due to adsorption of negolyte on the membrane.



Figure S26. Optical photograph of the Nafion 212 membrane from the 10 mM BCPIP-Co(II) symmetric cell at pH 3.5 after 100 cycles.

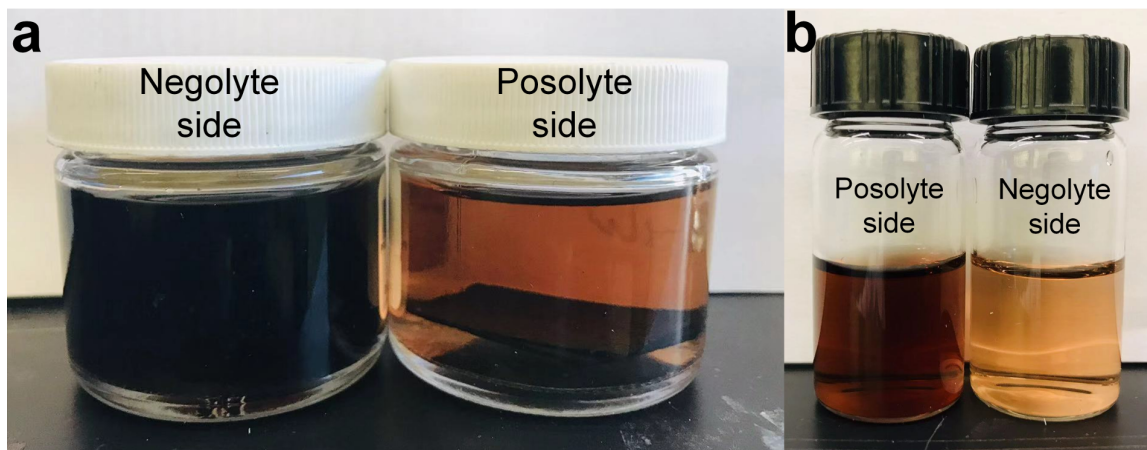


Figure S27. (a) Carbon papers removed from both posolyte and negolyte sides from the 10 mM BCPIP-Co(II) symmetric cell at pH 3.5 after 100 cycles, after soaking in ultrapure 18 M Ω ·cm water overnight. (b) The posolyte and negolyte solutions diluted 15x with ultrapure 18 M Ω ·cm water, from the 10 mM BCPIP-Co(II) symmetric cell at pH 3.5 after 100 cycles.

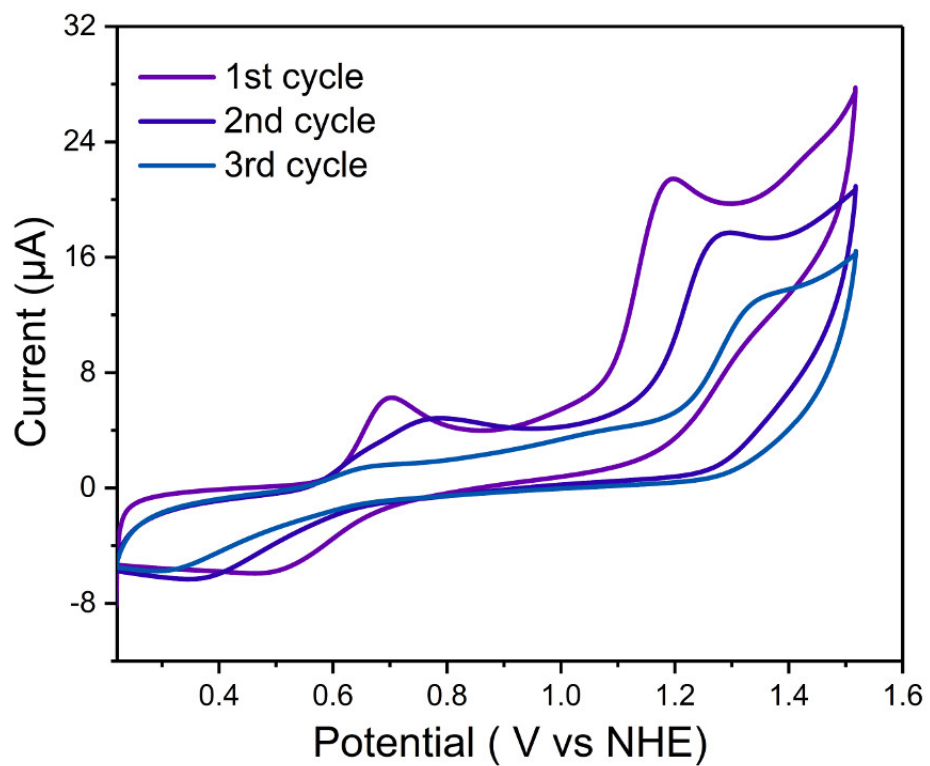
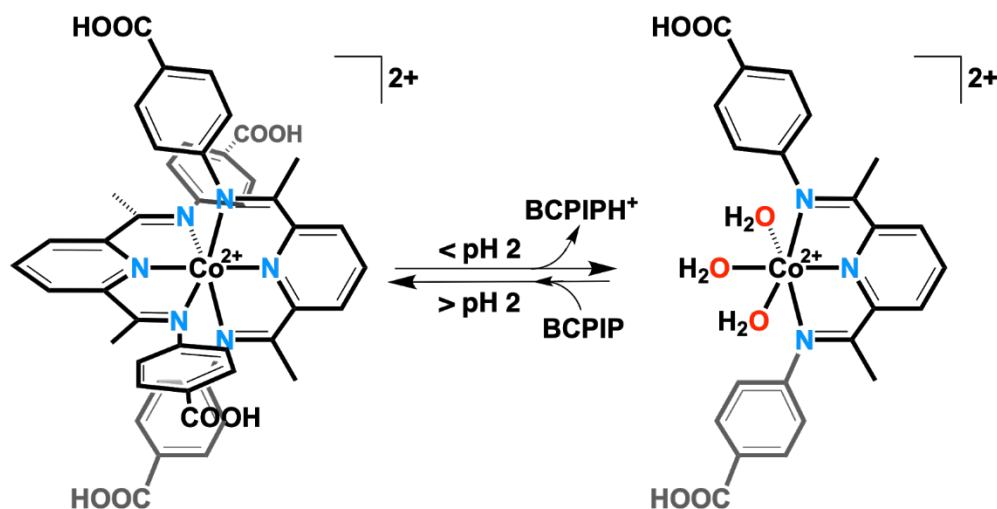


Figure S28. CV cycling of 1 mM of BCPIP-Co(II) in 0.5 M NaCl (aq) at pH 2.5 over an extended voltage window from 0.3 to 1.5 V vs NHE.

Table S1. Solubility of BCPIP-Co(II) complex at different pH values, corresponding to the subsequent neutralization of the four carboxylic groups.

pH	Solubility
1.9 (no addition of NaOH)	0.28 M
2.8 [one equivalent of NaOH/ BCPIP-Co(II)]	0.08 M
4.0 [two equivalents of NaOH/ BCPIP-Co(II)]	0.04 M
5.0 [3 equivalents of NaOH/ BCPIP-Co(II)]	0.18 M
6.3 [4 equivalents of NaOH/ BCPIP-Co(II)]	> 0.5 M (solution becomes very viscous and thus an upper limit could not be determined)



Scheme S1. Proposed equilibrium for the BCPIP-Co(II) complex in aqueous acidic environments $> \text{pH } 2$ and $< \text{pH } 2$. Below $\text{pH } 2$, protonation of the BCPIP would be expected, leading to replacement of the tridentate ligand with 3 aquo ligands.

In Figure 2b in the main text, it is noted that there is a cathodic peak at ca. -0.24 V for the solution of $\text{pH } 1.5$, prior to the Co(II)/Co(I) reduction peak at -0.34 V , which we believe results from dissociation of one ligand, leading to the trihydrate complex shown below (Scheme S1). Similar behaviour has been observed with cobalt bipyridine complexes, “The bpy ligand does not strongly bind to the cobalt center and dissociates in an acidic aqueous environment. There is an equilibrium between the diaqua $[\text{CoII}(\text{bpy})_2(\text{OH}_2)_2]^{2+}$ and $[\text{CoII}(\text{bpy})_3]^{2+}$ species.”⁵

Section S4: Crystallographic data for BCPIP-Co

Purple crystals of BCPIP-Co(II) were grown by solvent diffusion of acetonitrile (top layer) into a concentrated methanol solution of BCPIP-Co(II). Thermal ellipsoid plots are shown in Figures S1-S3. A purple crystal with the dimensions 0.63 x 0.29 x 0.24 mm³ was coated with a thin layer of hydrocarbon oil (Paratone-N) and then mounted on a glass fiber before being quickly placed in a low-temperature stream of N₂ on the X-ray diffractometer.⁶ With the crystal cooled to -100 °C, all data were collected by Cu K α radiation on a Bruker D8 equipped with APEX II CCD detector. The data were corrected for absorption from the indexing of the crystal faces based on Gaussian integration. The structures were solved by intrinsic phasing (SHELXT-2014)⁷ and refined using full-matrix least-squares on F² (SHELXL-2017).⁷ Non-hydrogen atoms are represented by Gaussian ellipsoids at the 30% probability level. The positions of hydrogen atoms were derived from attached carbon and oxygen atoms.

Table S1. Crystallographic Experimental Details**A. Crystal Data**

CCDC	1954971
Formula	C ₁₅₀ H ₁₃₀ C ₁₄ Co ₃ N ₂₄ O ₂₄
formula weight	2971.36
crystal dimensions (mm)	0.63 × 0.29 × 0.24
crystal system	orthorhombic
space group	<i>Aba</i> 2 (No. 41)
unit cell parameters ^a	
<i>a</i> (Å)	13.2673(3)
<i>b</i> (Å)	66.3212(15)
<i>c</i> (Å)	19.2434(5)
<i>V</i> (Å ³)	16932.3(7)
<i>Z</i>	4
ρ_{calcd} (g cm ⁻³)	1.166
μ (mm ⁻¹)	3.406

B. Data Collection and Refinement Conditions

diffractometer	Bruker D8/APEX II CCD ^b
radiation (λ [Å])	Cu K α (1.54178) (microfocus source)
temperature (°C)	-100
scan type	ω and ϕ scans (1.0°) (5-20-40 s exposures) ^c
data collection 2θ limit (deg)	157.92
total data collected	95826 ($-16 \leq h \leq 16$, $-80 \leq k \leq 82$, $-23 \leq l \leq 23$)
independent reflections	15815 ($R_{\text{int}} = 0.0750$)
number of observed reflections (<i>NO</i>)	13322 [$F_o^2 \geq 2\sigma(F_o^2)$]
structure solution method	intrinsic phasing (<i>SHELXT-2014</i> ^d)
refinement method	full-matrix least-squares on F^2 (<i>SHELXL-2017</i> ^e)
absorption correction method	Gaussian integration (face-indexed)
range of transmission factors	0.1042–0.0152
data/restraints/parameters	15815 / 1 / 937
Flack absolute structure parameter ^g	0.240(6)
goodness-of-fit (<i>S</i>) ^h [all data]	1.052

final R indicesⁱ

$R1 [F_o^2 \geq 2\sigma(F_o^2)]$	0.0610
$wR2$ [all data]	0.1446
largest difference peak and hole	0.532 and $-0.581 \text{ e } \text{\AA}^{-3}$

^aObtained from least-squares refinement of 9459 reflections with $5.32^\circ < 2\theta < 145.10^\circ$.

^bPrograms for diffractometer operation, data collection, data reduction and absorption correction were those supplied by Bruker.

^cData were collected with the detector set at three different positions. Low-angle (detector $2\theta = -33^\circ$) data frames were collected using a scan time of 5 s, medium-angle (detector $2\theta = 75^\circ$) frames using a scan time of 20 s, and high-angle (detector $2\theta = 117^\circ$) frames using a scan time of 40 s.

^dSheldrick, G. M. *Acta Crystallogr.* **2015**, *A71*, 3–8. (*SHELXT-2014*)

^eSheldrick, G. M. *Acta Crystallogr.* **2015**, *C71*, 3–8. (*SHELXL-2017*)

^fAttempts to refine peaks of residual electron density as disordered or partial-occupancy solvent oxygen or carbon atoms were unsuccessful. The data were corrected for disordered electron density through use of the *SQUEEZE* procedure as implemented in *PLATON* (Spek, A. L. *Acta Crystallogr.* **2015**, *C71*, 9–18. *PLATON* - a multipurpose crystallographic tool. Utrecht University, Utrecht, The Netherlands). A total solvent-accessible void volume of 831 \AA^3 with a total electron count of 170 (consistent with 9.5 molecules of solvent methanol, or 0.8 molecules per formula unit of solvent methanol molecule) was found in the unit cell.

^gFlack, H. D. *Acta Crystallogr.* **1983**, *A39*, 876–881; Flack, H. D.; Bernardinelli, G. *Acta Crystallogr.* **1999**, *A55*, 908–915; Flack, H. D.; Bernardinelli, G. *J. Appl. Cryst.* **2000**, *33*, 1143–1148. The Flack parameter will refine to a value near zero if the structure is in the correct configuration and will refine to a value near one for the inverted configuration. The value observed herein is indicative of racemic twinning, and was accommodated during the refinement (using the *SHELXL-2014* TWIN instruction [see reference *e*]). Thus the Flack parameter is provided for informational purposes only.

^h $S = [\sum w(F_o^2 - F_c^2)^2 / (n - p)]^{1/2}$ (n = number of data; p = number of parameters varied; $w = [\sigma^2(F_o^2) + (0.0413P)^2 + 34.3199P]^{-1}$ where $P = [\text{Max}(F_o^2, 0) + 2F_c^2]/3$).

ⁱ $R1 = \sum ||F_o| - |F_c|| / \sum |F_o|$; $wR2 = [\sum w(F_o^2 - F_c^2)^2 / \sum w(F_o^4)]^{1/2}$.

REFERENCES

- (1) Evans, D. F. 400. The Determination of the Paramagnetic Susceptibility of Substances in Solution by Nuclear Magnetic Resonance. *J. Chem. Soc.* **1959**, 0, 2003–2005.
- (2) Bard, A. J. *Electrochemical Methods : Fundamentals and Applications*, 2nd ed.; Wiley, New York: 2001.
- (3) Nicholson, R. S. Theory and Application of Cyclic Voltammetry for Measurement of Electrode Reaction Kinetics. *Anal. Chem.* **1965**, 37, 1351–1355.
- (4) Lavagnini, I.; Antiochia, R.; Magno, F. An Extended Method for the Practical Evaluation of the Standard Rate Constant from Cyclic Voltammetric Data. *Electroanalysis* **2004**, 16, 505–506.
- (5) L. Tong, L. Duan, A. Zhou and R. P. Thummel, *Coordination Chemistry Reviews*, **2020**, 402.
- (6) Hope, H. X-Ray Crystallography: A Fast, First-Resort Analytical Tool. In *Progress in Inorganic Chemistry*; John Wiley & Sons, Ltd, 2007; pp 1–19.
- (7) Sheldrick, G. M. SHELXT – Integrated Space-Group and Crystal-Structure Determination. *Acta Cryst A* **2015**, 71, 3–8.